Video Measurements of Fluid Velocities and Water Levels in Breaking Waves

K. Govender[1]*, M. J. Alport[2]†, G. Mocke[3] and H. Michallet[4]

[1]Department of Physics, School of Physical Sciences, University of Durban-Westville, South Africa
[2]School of Pure and Applied Physics, University of Natal, Durban, South Africa
[3]Coastal Development and Marine Resources Programme, ENVIRONMENTEK, CSIR, Stellenbosch, South Africa
[4]Laboratoire des Ecoulements Geophysiques, Grenoble, France

Abstract

The cost-effective measurement of the velocity flow fields in breaking water waves, using particle and correlation image velocimetry, is described. The fluid velocities are estimated by tracking the motion of neutrally buoyant particles and aeration structures. Results of the phase-ensemble-averaged velocity flow fields, time-averaged horizontal velocities and turbulence results are presented for laboratory waves breaking on a beach of slope 1:20 and for waves breaking over a submerged bar. A comparison of measurements using video and LDA techniques is also presented. The measurement of water levels and wave roller structures is accomplished by generating a video time series of the wave at a given horizontal position, from which the water levels and rollers structures are extracted.

1. Introduction

Deep-water ocean waves propagating towards a sloping beach begin to slow down as they move into shallow water. This is accompanied by a corresponding increase in wave height, referred to as shoaling. Further increase in wave height occurs as the waves move up the beach, until a point is reached at which breaking occurs. Breaking is characterised by the tip of the crest falling onto the front face of the wave, forming a body of water that rides on the face of the wave. This body of water is called the roller. The roller is transported shore-wards and there is a corresponding return flow beneath the wave called the undertow. The wave breaking also generates turbulence, which is responsible for the suspension of sediments. These suspended sediments are then transported, in 2D wave propagation, to the breakpoint, resulting in beach erosion and coastline changes. The accumulation of sediment at the breakpoint also results in the formation of a sand-bar at that point, which in turn influences the breaking process.

In order to predict beach erosion and coastline changes it is therefore necessary to have a detailed knowledge of the internal and external properties of shoaling and breaking waves. The external property is the elevation of water level with respect to time and the basic internal property of the wave is the evolution of the velocity flow field. Other internal parameters, such as the time-averaged current and turbulence levels, can then be derived from this velocity field.

Traditionally, the time series of the surface wave is measured using partially submerged resistance or capacitance wave gauges. In order to measure the time series over

a large area, it is necessary to use a number of gauges or alternatively to make measurements sequentially using a single gauge. This can be a tedious exercise and conceivably gauges can interfere with the local flow behaviour. The performance of these gauges in the surf zone is also often unreliable due to the highly aerated water and rapid evolution of the air-water interface.

The fluid velocity is usually measured using either a mechanical propeller, electromagnetic flow-meters, hot-wire anemometer or Laser Doppler Anemometry (LDA). LDA is an interferometric technique that provides a velocity measurement at a single point and has sufficient frequency resolution in order to measure the rapid fluctuations of fluid velocities in turbulent flows. None of the above techniques can however provide an instantaneous snapshot, that is, a spatially extended synoptic view of the flow field. Secondly, LDA systems in particular are labour intensive to setup and the equipment required is costly. The conventional LDA also fails due to signal dropout when there is a large concentration of air bubbles in the measurement area, such as in the surf zone, although this problem has been alleviated somewhat through the use of fibre optics [1].

Recently there has also been a growing interest in the use of imaging techniques to measure wave parameters in the laboratory and in the ocean. A number of researchers have reported on the measurement of water surface elevation using specular reflection of the water surface [2,3]. This type of measurement is suitable for the study of the spectral-wavenumber characteristics of waves in scaled model facilities and at sea. There has also been serious interest in the application of optical techniques to the measurement of velocities within a breaking wave [4] and in the surf zone [5–7].

In this paper we report on the video measurements of fluid velocities, the time series of the water level and roller structure in laboratory water waves breaking on a plane beach of slope 1:20 and also in waves breaking over a submerged bar. The fluid velocities are measured using digital correlation image velocimetry (DCIV) [8,9], and the time series of the water level and roller structures are measured by tracking the evolution of the air-water interface and aeration in a video time series of the wave.

The DCIV technique involves capturing the instantaneous image of a large number of submerged neutrally buoyant seeds at two or more time instances. The velocity is then computed using the displacements that these particles have

*e-mail: kgovend@pixie.udw.ac.za
†e-mail: alport@ph.und.ac.za

incurred over the known time intervals. This clearly requires the existence of particles to be imaged in the field of view, and a method of recording and processing these images. There are essentially two types of possible image analysis techniques: in situations where the density of seed particles are low, individual tracking of particle images is required, whilst in cases of high seed densities, 2D cross correlation techniques are employed to track the image of a group of particles. The results presented in this paper have been obtained using the 2D cross-correlation techniques.

The time series of water elevation was measured by imaging the wave from the side and exploiting the gradient in the grey level intensity of the image across the air-water interface. The time series at a particular position is obtained by first generating a keogram from a video recording of the wave. This technique is also used to estimate the size of the roller formed in the bore of the wave during breaking. The concept of keograms and the method of extracting the time series of the wave are explained in Section 2.

The experimental set-up and procedures are discussed in Section 2. Results of phase-ensemble-averaged and instantaneous velocity flow fields for a spilling wave breaking on a plane slope beach and over a submerged bar are provided in Section 3.

2. Experimental setup and procedures

The experiments were conducted using wave flumes at two different laboratories. Firstly, experiments on waves breaking on a beach of slope 1:20 was conducted in a 2D glassed walled wave flume at the Coastal Engineering Laboratory, CSIR, Stellenbosch, South Africa. Figure 1(a) depicts the schematic of the flume showing the plane slope beach and the measurement positions. The flume is 20 m long, 1 m deep and 0.7 m wide, and fitted with a well supported wooden beach having a slope of 1:20.

A second experiment investigating the breaking of waves over a submerged bar was conducted in the wave flume at the Laboratoire des Ecoulement Geophysique et Industrials, Grenoble, France. Figure 1(b) shows the schematic
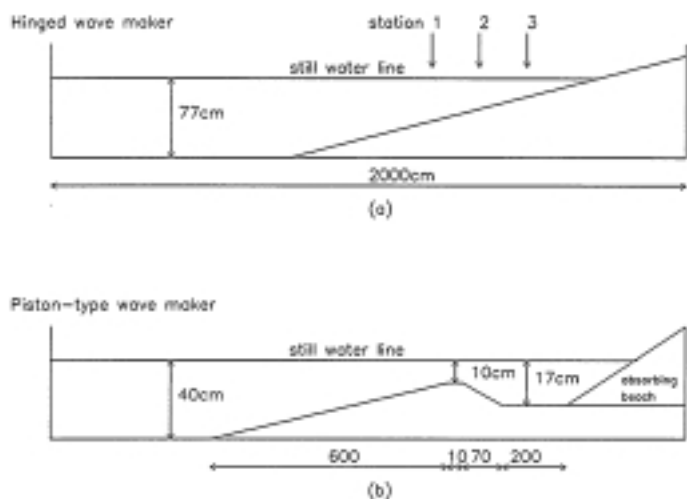

Fig. 1. (a) Schematic of the flume showing 1:20 plane slope beach. Velocity flowfields measured at stations 1-3 located at 4.36, 3.38 and 2.39 m relative to the still water mark on the beach. (b) Schematic of flume with a bottom profile resembling a submerged bar. The bar consists of a 1:20 upslope followed by a 10 cm flat section and a 1:10 downslope.

of the flume and the bottom profile. The bar consists of a 1:20 upslope followed by a 10 cm flat section and then a 1:10 down slope. The wave condition was adjusted such that breaking occurred at the top of the up slope. Velocity flow field measurements were conducted on the downslope and flat section following the downslope.

2.1. *Velocity flow field measurement procedure*

The flume was seeded with neutrally buoyant particles and a rectangular light sheet was used to illuminate a longitudinal section of the flume. The light sheet, which is approximately 1 cm wide, was located about 14 cm away from the side glass. A strobe light was used as a source for the light sheet and a non-interlaced progressive scan digital camera, connected to a frame grabber residing in a PC, was used to record images of illuminated particles directly to the hard disk. The non-interlaced camera provides a high spatial resolution (764×468 pixels) image. It is possible to obtain pairs of images, with sampling times ranging from a few microseconds to a few milliseconds, while still using the normal (60 Hz) frame update rate, by strobing the light sheet at the end of one frame time and then again at the beginning of the next frame time. Since the sequence of the images is known, the 180 degree directional ambiguity, usually associated with multiple strobing during a single frame time, is removed.

It was discovered, after experimenting with a number of macroscopic particles, that un-expanded polystyrene beads, which were heated in water at a temperature of around 86°C for approximately 30 s, were most suitable. These partially expanded beads, which are approximately 0.8 mm in diameter, function well as seed particles since they are almost neutrally buoyant and their white matt surface makes them good point source scatterers.

The displacement of the seed and aeration structures between the two images was estimated using 2D cross-correlation. The correlation technique involves finding matching structure between two images and therefore requires high seed densities. The presence of non-matching seeds or seed patterns between images simply contributes to noise. Provided the signal-to-noise ratio of the matching structures is large enough, the peak of the computed cross-correlation function is a good estimate of the displacement of that particular structure. The cross correlation can be computed in the spatial domain by explicit evaluation of the 2D cross correlation function [9] or in the spectral domain by computing the cross spectral density function and transforming back into the spatial domain using the 2D FFT [8].

The cross correlation of the images in the Fourier domain is performed as follows: Each image frame is sub-divided into smaller 32×32 pixel sub-images, and transformed into the Fourier domain using a 2D FFT algorithm. The FFT of a sub-image in the first frame is multiplied by the conjugate of the FFT of the corresponding sub-image in the second frame, which is then transformed back into the spatial domain as given below.

$$R_{fg}(u, v) = F(u, v) \cdot G^*(u, v),$$

$$r_{fg}(m, n) = FFT^{-1}\{R_{fg}(u, v)\}$$

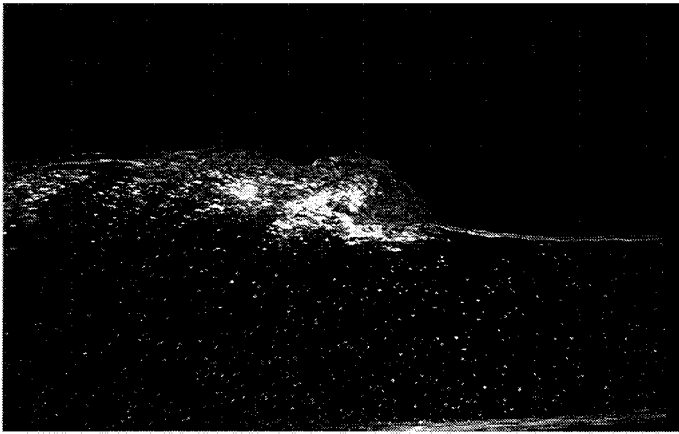where $F(u, v)$ is the Fourier transform of the sub-image,

Fig. 2. Image of the crest of a spilling wave at 2.2l m (station 3) beyond the breakpoint, showing neutrally buoyant particles and aeration.

direction to a size of 32×32 pixels, resulting in a border of zero intensity around the original 12×18 pattern box. The search area, that is the corresponding region in the second frame where a match with the sub-image in the first frame is likely to occur, can be a full 32×32 sub-image centred at (k, l) in the second frame. The co-ordinates of the peak, in the cross-correlation result, represent the displacement of the original 12×18 pattern box. The zero padding does not influence the cross correlation result. In fact, the zero padding eliminates some of the problems associated with implementing cross correlation using the FFT, such as wrap around [10].

2.1.1. *Sub-pixel resolution.* Estimation of the position of the peak in the cross correlation using peak intensity gives the position accurate to within ± 0.5 of the pixel separation. The position of the peak was estimated to sub-pizel resolution as described below.

The intensity profile in the horizontal and vertical direction about the peak was Fourier transformed using an FFT of length N_1, where N_1 is the sample length of the intensity profile. The spectrum is then zero padded to a length N_2, where $N_2 > N_1$, and the inverse Fourier transform computed using an inverse FFT of length N_2 to give the interpolated intensity profile in the respective directions. An interpolation factor of N_2/N_1 is achieved. In our application an interpolation factor of $64/1$ was used. We will refer to this form of interpolation as the Fourier interpolation method. This method approaches the ideal reconstruction of an analogue signal from its digital samples [10]. A peak search using the Fourier interpolated intensity profile in the x and y direction gives the position of the peak accurate to within the interpolated pixel spacing, which is finer than the pixel spacing of the raw data.

2.2. *Water level measurement procedure*

The measurement of the time series of the water level was accomplished by imaging the wave from the side with the
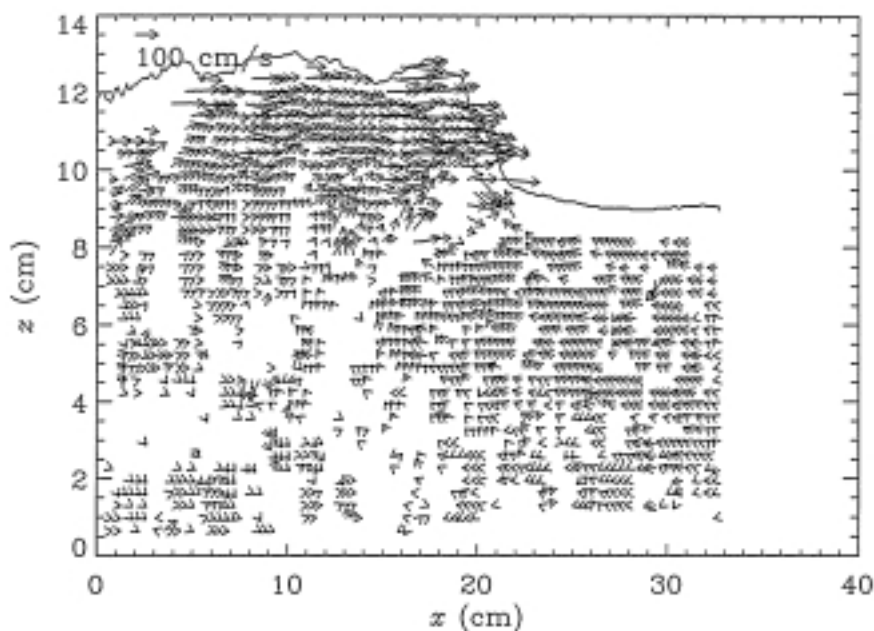
$f(m, n)$, in the first video frame, $G^*(u, v)$ is the conjugate of the Fourier transform of the corresponding sub-image, $g(m, n)$, in the second frame, and $r_{fg}(m, n)$ is the computed 2D cross correlation function of the sub-images. The intensity profile along the x and y directions about the peak in the computed cross-correlation is then interpolated using the Fourier interpolation method discussed in the next section. The displacement of each sub-image is thus estimated to within the interpolation factor, i.e. typically $1/64$, of the original pixel spacing.

When using 2D FFT algorithms, it is beneficial to use sub-images having sizes that are powers of two. This, however, does not necessarily preclude the computation of the displacement of a sub-image whose dimensions are not a power of two. This is achieved as follows: Typically a smaller sub-image from the first frame, say 12×18 pixels, about some point (k, l), is selected. This odd-sized sub-image is then adjusted, such that it has a zero mean, and then zero padded in the horizontal and vertical

Fig. 3. Instantaneous velocity vector flow field obtained using the 2D cross correlation method.
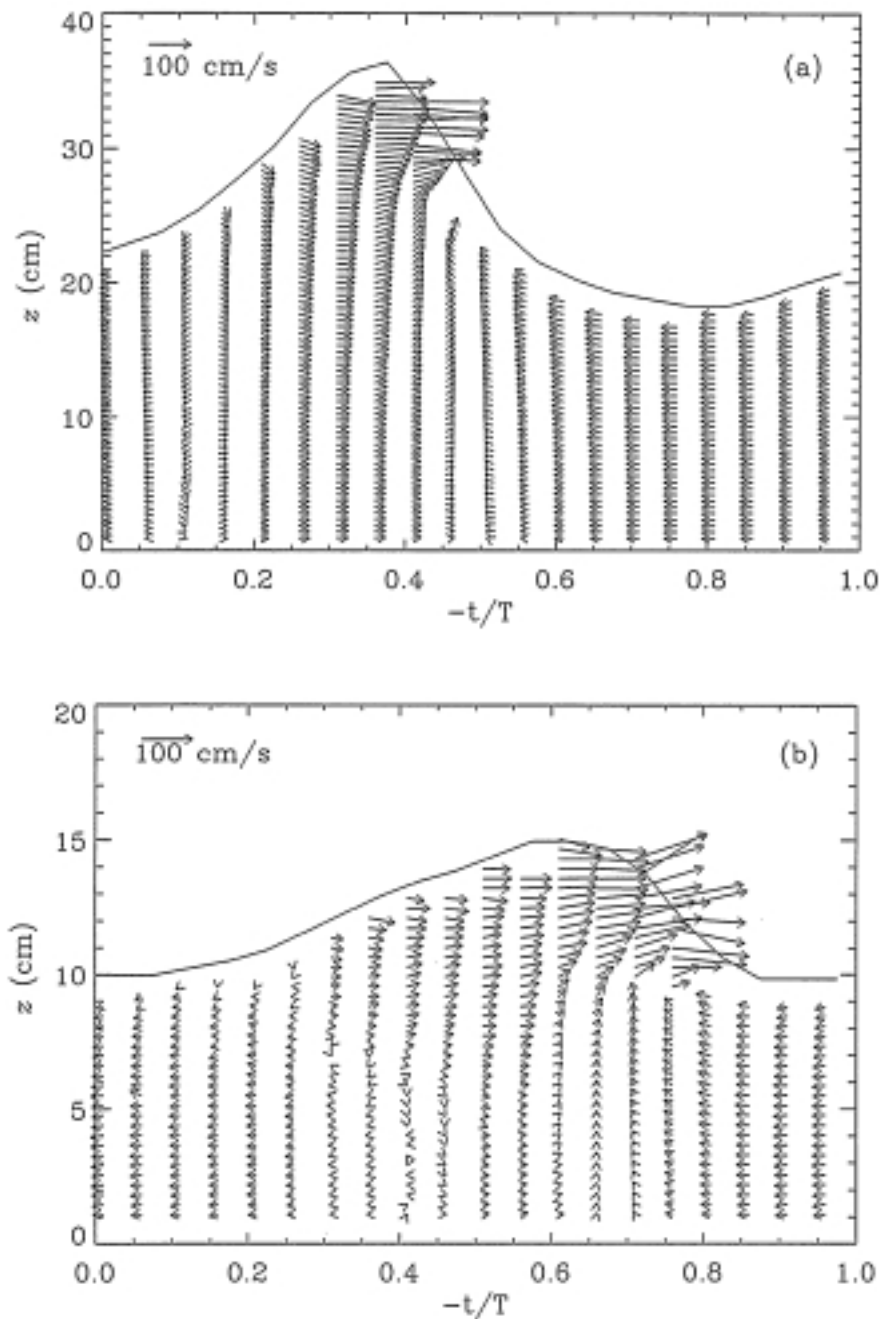
Fig. 4. Phase-ensemble-averaged velocity flow field of a 0.9 Hz spilling wave measured at (a) station 1 and (b) station 3 which correspond to 0.24 m and 2.21 m beyond the breakpoint, respectively. A 100 cm/s scale vector is drawn. z represents vertical distance measured from the bottom upwards and t/T represents the fraction of a wave period.

camera located at the height corresponding to the still water level and the wave was illuminated from above. A black backing sheet was placed at the rear of the flume. This arrangement allows the air-water interface to be identified by locating the resulting sharp transition in the vertical grey scale intensity, and also enhances the presence of aeration as a result of wave breaking. The camera was also mounted on a base that could be translated on a set of rails parallel to the flume.

The time series of the water level was extracted using the following procedure: At each position along the flume a video recording of the wave was made. A single vertical line of pixels at a fixed position was then extracted from a sequence of images. These vertical samples were then stacked side by side to create a new image, called a keogram.

A robust cross correlation algorithm was then used to determine the position of the air-water interface, resulting in the time series of the wave.

The keogram technique was also used to measure the geometry of the roller and the aerated region of the wave in the surf zone. This was achieved by first forming a phase-ensemble-averaged keogram of the wave and demarcating the high intensity aerated region which was identified as being the roller or aerated region.

3. Results and discussion

3.1. *Velocity flow field measurements*

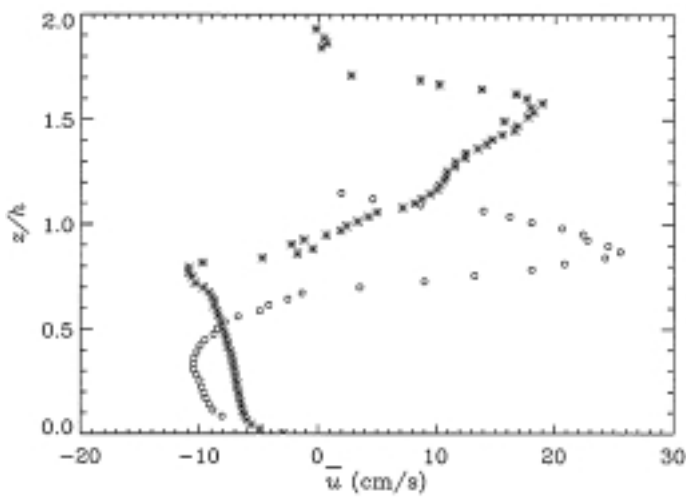Velocity flow field measurements are provided, firstly, for a 0.9 Hz spilling-wave having a deep water wave height of

Fig. 5. Time-averaged horizontal velocity component, $\bar{u}$, as a function of distance above the bottom, z/h, at 0.24 m (*) and at 2.21 m (○) beyond the break point for the spilling wave. These were obtained by time-averaging the phase-ensemble-averaged flow fields in Figs. 4(a) and (b). The vertical distance above the bottom is non-dimensionalized with respect to the mean local water depth, h.
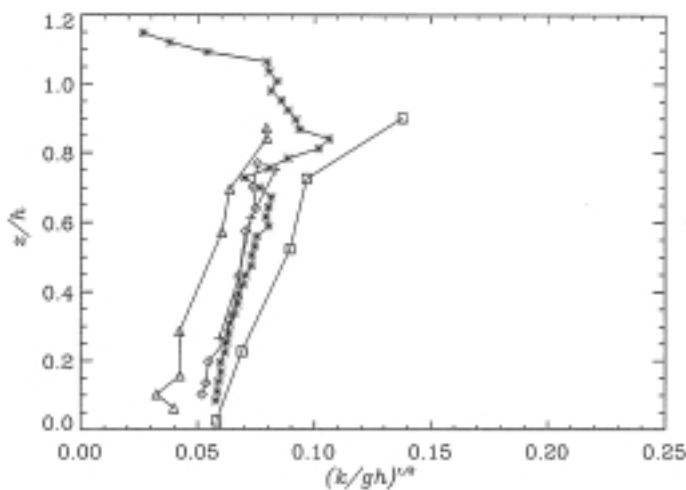

Fig. 6. Comparison of the Froude scaled time-averaged turbulent kinetic energy of Stive (+) [11], Ting and Kirby (◇) [12], Cox *et al.* (△) [13], Okayasu (□) [14], and our DCIV (*) measurements in the spilling wave, breaking on a 1:20 slope beach, at station 3. The vertical axis is normalised with respect to the mean local water depth, h.

16 cm and breaking on a plane beach of slope 1:20. Figure 2 shows an image of the crest of the spilling wave approximately 2.21 m (station 3) beyond the break point, captured using the DCIV setup. This image, which is one of a pair captured 1 ms apart, shows a scene containing both bubbles resulting from the wave breaking, and polystyrene seed particles. It was found that the structure of corresponding portions of the two images persists for the duration of the sampling time with very little or no distortion. The calculated velocity vector field, using DCIV, for the above image pair in question is shown in Fig. 3. Peak velocities of ~2 m/s occur near the surface, while near the bottom the velocities are almost zero, therefore the vectors have very small or no tail. Also evident in Fig. 3, are regions where no velocity estimates exist. This is due to a lack of seed or aer-

ation structures. These gaps in the measurement are quite easily filled by averaging over a number of wave cycles. The rise velocity of the air bubbles in this highly turbulent flow regime is negligible in comparison to the velocity components of the flow. It is thus possible to obtain a flow pattern well into the aerated region of the wave using the air bubbles to create the necessary structure. In the past, researchers have gone to great lengths to remove the effects of the air bubbles in order to highlight particulate matter that has been deliberately added to the flow. In lower velocity streamline laminar flow, however, it would be necessary to obtain an estimate of the rise velocity of the bubbles and apply the necessary correction to the flow field. The sampling time is determined by satisfying the competing criteria of requiring a persistent bubble structure as well as a measurable displacement.

Figures 4(a) and (b) illustrate the phase-ensemble-averaged velocity flow field at 0.24 m (station 1) and 2.21 m (station 3), respectively, beyond the break point for the 0.9 Hz spilling-wave breaking on a plane beach. Each vector in these figures has been computed using instantaneous velocity estimates measured over at least 50 wave cycles. There are a number of features that are clearly visible from these figures; The profile of the wave is cnoidal shaped near the break point and more saw-toothed further in the surf zone. The velocity streamlines near the break point are almost symmetrical about the crest. The velocity streamlines further into the surf zone are more asymmetrical with a point of inflexion of the flow vectors occurring at the peak of the wave. Measurements by Stive [11], using LDA, on spilling-waves breaking on a 1:40 slope beach indicate peak velocity magnitudes, near the breakpoint, of 60 cm/s at positions in the middle of the crest, while in the trough the peak velocities are in the order of 30 cm/s, which are similar to those in Fig. 4(a). Further in the surf zone, peak velocity magnitudes of 25 cm/s in the crest and 20 cm/s in the trough of the wave were measured by Stive, which are slightly lower compared to those presented in Fig. 4(b).

Figure 5 shows the time-averaged horizontal velocity, $\bar{u}$, as a function of depth, derived from Fig. 4(a) and (b). The reverse flow below the approximate level of the trough ($z/h \sim 0.7$) reflects the undertow, while the flow above the trough is due to the mass flux in the crest of the wave. There is maximum forward time-averaged velocity of 20 cm/s and 25 cm/s at stations 1 and 3, respectively. Near the breakpoint a maximum undertow velocity of approximately 10 cm/s occurs near the trough level, while further in the surf zone a maximum undertow of approximately 10 cm/s occurs closer to the bottom. Undertow measurements by Ting and Kirby [12] in spilling-waves breaking on a 1:35 slope beach indicate peak undertow velocities of approximately 7 cm/s near the breakpoint and 10 cm/s for corresponding positions in the surf zone. Thus, the measurements presented here are of similar magnitude to those made by other researchers using similar test conditions. Previous measurements of the time averaged flow [13–15], using the more conventional flow measuring methods, have only been available for measurements below the trough level. The time-averaged horizontal flow presented here show measurements above the trough level, although with a much higher forward mass flux. This is due to the lower fluid density in the wave crest as a result
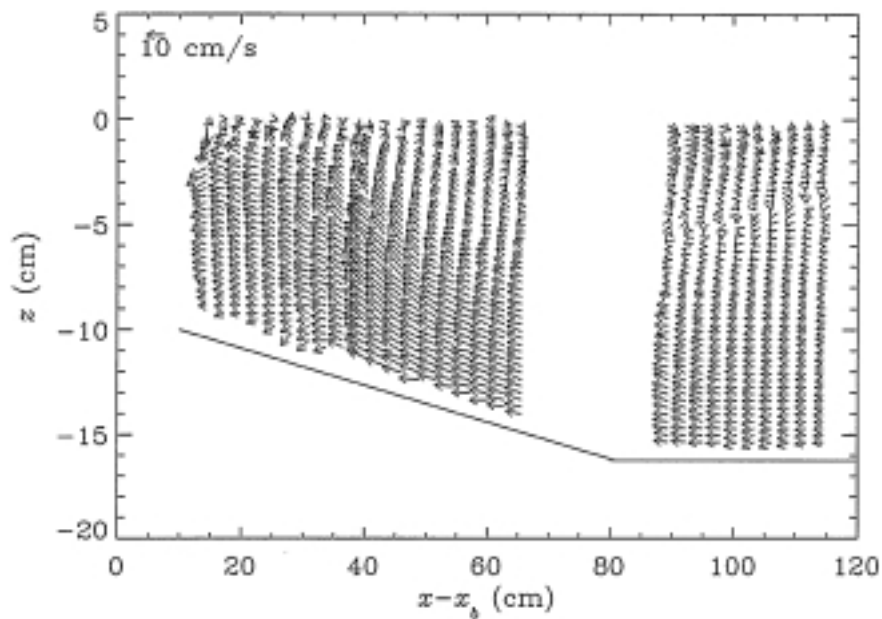
Fig. 7. Time-averaged flow field in 0.67 Hz waves breaking over a submerged bar. The solid line represents the profile of the bed.

of wave breaking. The time-averaged velocity is important in the study of sediment transport within the surf zone.

The phase-ensemble-averaged turbulent kinetic energy, k, was computed using two components of the measured velocity using [15]

$$k = 1.33 \frac{1}{2}(u'^2 + w'^2)$$

where u' and w' are the horizontal and vertical velocity fluctuations about the phase-ensemble-averaged velocities. The time-averaged turbulent kinetic energy was obtained by averaging across the wave phase at each vertical position.

The non-dimensionalized time-averaged turbulent kinetic energy at station 3, together with other existing LDA measurements, is shown in Fig. 6. The measured profiles, as extracted from Mocke [16], correspond to surf zone positions where $h/h_b \sim 0.7$, and are normalised using a Froude scaling. It can be seen that, below the trough level, the turbulent kinetic energy measurements presented here are consistent with those of Stive [11] and Ting & Kirby [12] and extend well above the trough level, unlike existing LDA measurements. Also evident from this measurement is the high level of turbulence kinetic energy above the approximate trough level.

Figure 7 shows the time-averaged flow field for the case of waves breaking over a bar (see Fig. 1(b)). This measurement represents waves having a deep water wave height of 7.4 cm and a frequency of 0.67 Hz. Measurements are provided only for positions below the still water line. It can be seen in Fig. 8 that a circulation is set-up as a result of breaking, that is, there is net reverse flow near the bottom and net forward flow above $z = -4$ cm on the flat section of the bed. This circulation is driven by a transfer of energy from the wave to the mean current. Near the breakpoint the mean reverse flow increases from the bed upwards, whereas further from the breakpoint the profile of the mean reverse flow has a parabolic shape with maximum flow (~ 10 cm/s) occurring near the bottom. There is a steady decay of reverse flow in

the flat section with increasing distance away from the breakpoint.

3.2. *Water level measurements*

Figure 8 shows a sample keogram of the spilling wave in the surf zone (at 3.6 m beyond the breakpoint) and the resulting time series is given in Fig. 9. A comparison of the time series of water levels obtained using the above video technique with those from a resistance wire gauge can be found in [5]. The detailed information on water levels measured at a large number of positions along the flume have been used for the validation of computational models of mean water level and wave heights [5].

The configuration of the aerated region, or roller, on the front face of the wave in the surf zone is of significance for determining energy dissipation rates as well as cross-shore fluxes of mass and momentum [17]. Measure-
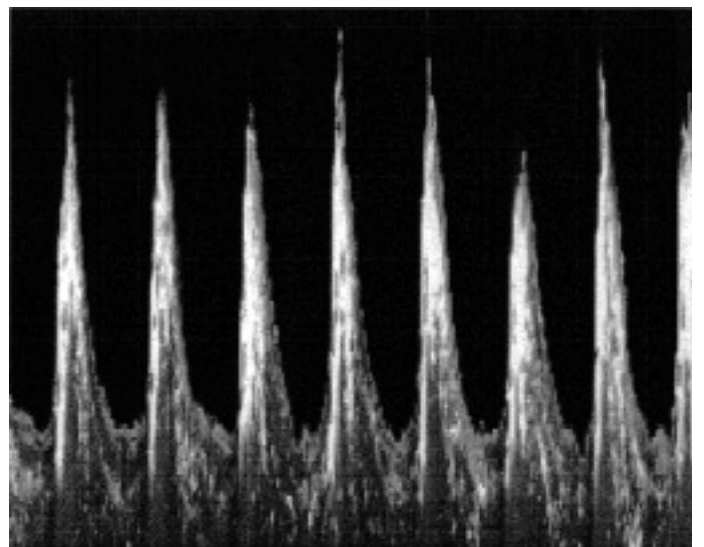

Fig. 8. Keogram of a spilling wave, breaking on a 1:20 plane slope beach, at 3.6 m beyond the breakpoint.
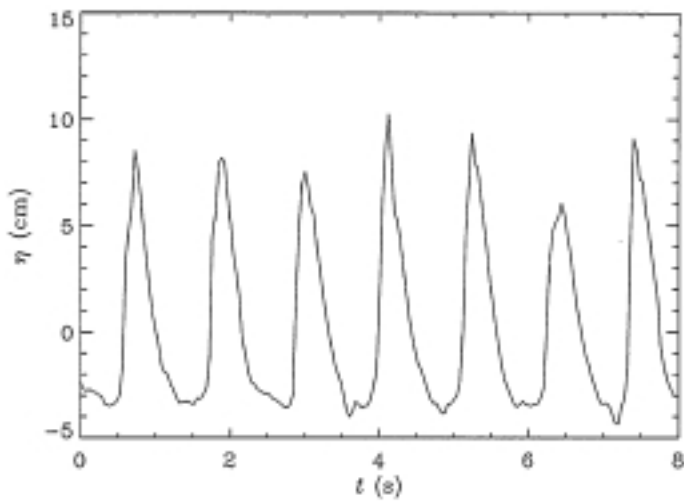
Fig. 9: Time series of the water level extracted from the keogram in Fig. 8.
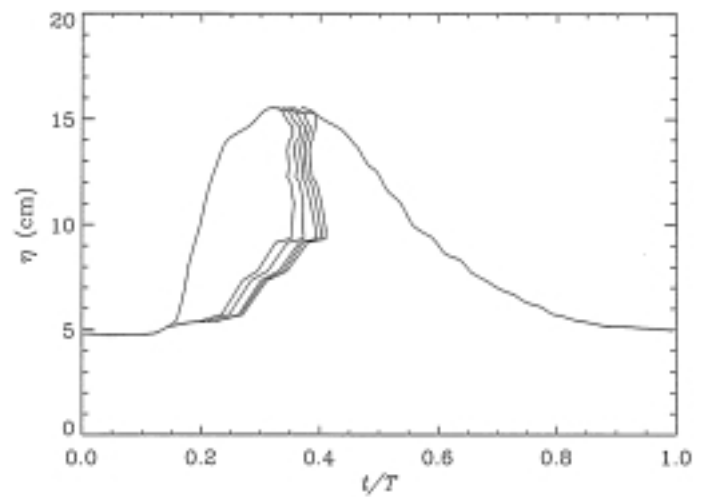
Fig. 11. An example of contours of aeration extracted from the phase-ensemble-averaged keogram in Fig. 10, obtained using greyscale thresholds.
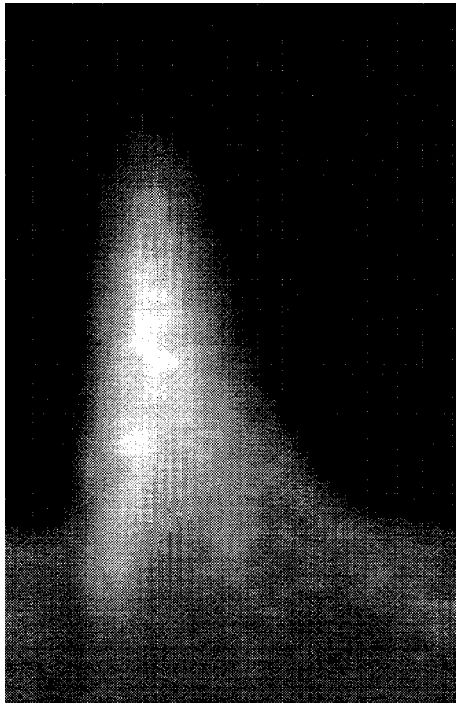

Fig. 10. Phase-ensemble-averaged keogram of the spilling wave illustrating aeration at 3.6 m beyond the breakpoint.
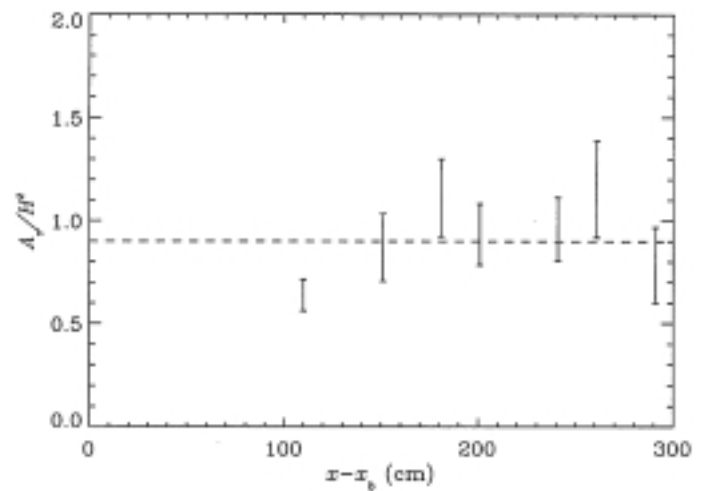

Fig. 12. The evolution of the normalised roller area, A_r/H^2, versus distance, $x - x_b$, from the breakpoint for spilling waves breaking on a 1:20 slope beach. The roller area is normalised with respect to H^2 at each position. The dashed line represents the estimate by Svendsen [17].

ments of the roller configuration in spilling-waves, breaking on a 1:20 plane slope beach, were performed at a number of positions in the surf zone.

Figure 10 depicts the phase ensemble-averaged keogram representation of images recorded at 3.6 m beyond the breakpoint in the spilling wave case. Although the aerated region at the front of the wave is easily seen, it is less clear how much of the bubble area actually constitutes the wave roller. A variable filter approach is therefore taken, whereby the roller area for variable levels of grey scale intensity are determined. This procedure produces a family of grey level contours as depicted in Fig. 11. These measurements were used to quantify the roller area across the surf zone.

Measured roller area (A_r) as a function of position in the surf zone relative to the breakpoint, x_b, and normalised with respect to the square of the wave height at each position, is

shown in Fig. 12. The lower and upper limits of each measurement in Fig. 12 correspond to the normalised roller area computed using two different intensity thresholds to determine the roller area in the phase averaged keogram. The lower estimate corresponds to a threshold, which is slightly below the maximum intensity in each keogram. The upper estimate corresponds to a threshold, which is slightly greater than the maximum intensity of the bubbles outside the roller area. The results of Fig. 12 shows that the normalised roller area for the spilling-wave increases from 0.6, near the breakpoint, to approximately 1 at 1.5 m beyond the breakpoint, and decreasing slightly thereafter. A similar measurement has been performed by Duncan [18] on a spilling waves created over a towed hydrofoil, and a constant ratio $A/H^2 = 0.9$ was estimated by Svendsen [17]. The waves breaking over a towed hydrofoil is of constant form at all

times, provided that the speed of the hydrofoil is constant. The surf zone, on the other hand, is characterised by a transition zone, just beyond the breakpoint, where there is a growth of the roller, followed by the inner surf zone with a fully developed bore. In the inner surf zone the mean roller area is ~ 0.9.

4. Conclusion

The cost-effective measurement of the velocity flow fields, temporal development of the water level and the roller geometries in a laboratory surf zone has been demonstrated by means of video techniques.

Various time series of the water levels, obtained by keogram analysis, have been measured at high cross-shore spatial resolution without having to introduce an array of potentially intrusive devices such as resistance gauges. The images have also provided quantitative information on wave roller areas, all of which are important parameters for modelling wave energy dissipation and undertow currents. Within the range of imposed thresholds, the normalised roller area (A_r/H^2) is found to be increasing as a function of distance from the breakpoint in the surf zone. By analyzing image structures composed of seeds and bubbles using correlation image velocimetry (DCIV), together with high speed strobing, velocity and turbulence flow fields over the full water depth have been obtained. To our knowledge, this is the first example of such high resolution measurements in the aerated roller area.

It was evident from the phase-ensemble-averaged velocity and turbulence kinetic energy measurements that the region of highest velocities and turbulence generation is located in the front part of the wave crest, in the vicinity of the wave roller. The increased development of the wave roller closer to the shore is associated with higher turbulence levels. Wave averaged horizontal velocities indicate that onshore mass fluxes above the trough level are higher than the offshore component below the trough. Wave averaged and non-dimensionalized turbulent kinetic energy levels were found to compare well with previous LDA measurements, which have been confined to levels below the wave trough. The significantly higher velocity and turbulence magnitudes found above this level in the current investigation highlights possible inadequacies in existing descriptions of the surf zone flow field.

References

1. Hino, M. *et al.*, Laser-doppler velocimetry and hot-wire/film anemommetry, 97 (1984).
2. Krishnan, K. S., Peppers, N. A., Proc. Intl. Symp. Ocean Wave Measurement and Analysis **2**, 113 (1974).
3. Jahne, B., Klinke, J. and Waas, S., J. Opt. Soc. Am. **A8**, 2197 (1994).
4. Quinn, P. A. *et al.*, Proc. Conf. Coastal Dynamics, (1995).
5. Govender, K. *et al.*, Proc. 6th Intl Symp Flow Modelling and Turbulence Measurements VI, (1996).
6. Craig, K. R., Thiek, R. J., Proc. ICCE'96, 602 (1996).
7. Chang, K., Philip, L .F. L., Proc. ICCE'96, 527 (1996).
8. Willert, C. E., Gilbert, M., Exp. Fluids **10**, 181 (1991).
9. Fincham, A. M., Speeding G. R., Exp. Fluids **23**, 449 (1997).
10. Oppenhiem, A. V. and Schafer, R. W., "Discrete-time signal processing", (Prentice Hall, 1989).
11. Stive, M. J. F., Proc. ICCE'80, 547 (1980).
12. Ting, F. C. and Kirby, J. T., Coast. Eng. **24**, 51 (1994).
13. Cox, D. T., Kobasahi and N., Okayasu, A., Coast. Eng. **98** (1994).
14. Okayasu, A., "Characteristics of turbulence structures and undertow in the surf zone", (PhD Thesis, Yokohama Nat. Univ. 1989).
15. Svendsen, I. A., Madsen, P. A., Bur Hansen, J., Proc. 16th Int. Coast. Eng. Conf. 520 (1978).
16. Mocke, G. P., CSIR report ENV/S-C 97069, (1998).
17. Svendsen, I. A., Coast. Eng. **8**, 303 (1984).
18. Duncan, J. H., Proc. R. Soc. Lond. **A377**, 331 (1981).